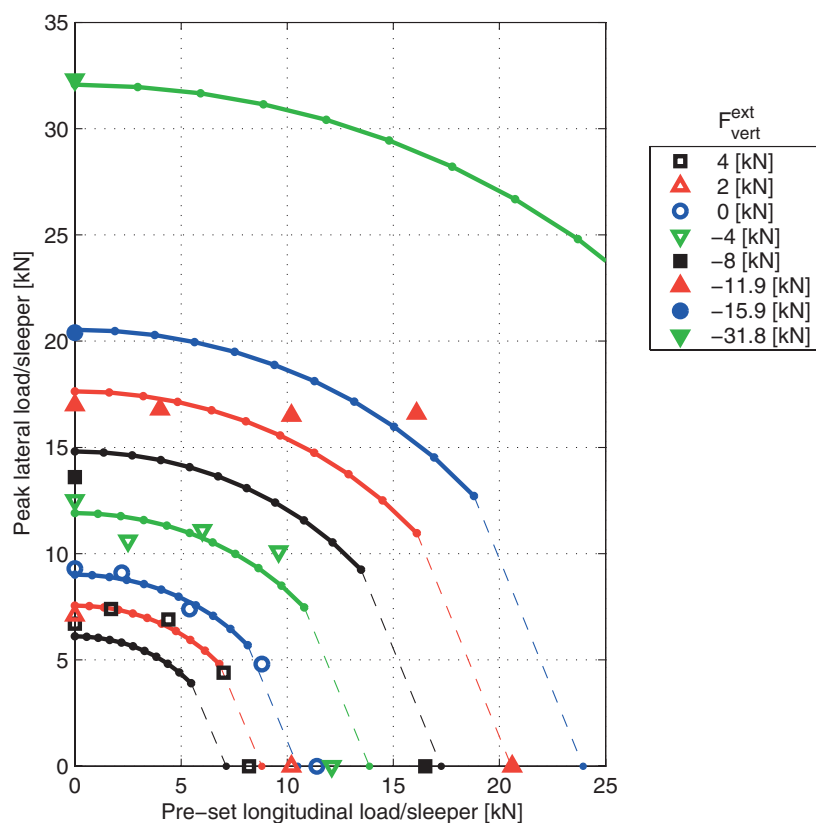


# A plasticity model for ballast resistance





Lars Jacobsson

# A plasticity model for ballast resistance

## Abstract

A constitutive model based on plasticity theory with a non-associative flow rule has been developed. The model is formulated in terms of sleeper displacements and forces, and includes hardening and softening controlled by irreversible transversal (lateral and longitudinal) sleeper displacements.

The model has been calibrated using results from lateral and longitudinal ballast resistance tests carried out in laboratory for a number of vertical load levels. Moreover, results from simulations of lateral ballast resistance tests with a superimposed longitudinal force for a number of vertical load levels were compared with experimental data. It is seen that there is a fair agreement between results from simulations and available experimental data.

Key words: constitutive modeling, plasticity model, ballast resistance, track buckling

**SP Sveriges Provnings- och  
Forskningsinstitut**  
SP Rapport 2005:27  
ISBN 91-85303-58-5  
ISSN 0284-5172  
Borås 2005

**SP Swedish National Testing and  
Research Institute**  
SP Report 2005:27

Postal address:  
Box 857,  
SE-501 15 BORÅS, Sweden  
Telephone: +46 33 16 50 00  
Telex: 36252 Testing S  
Telefax: +46 33 13 55 02  
E-mail: [info@sp.se](mailto:info@sp.se)

# Contents

<b>1</b>	<b>Introduction</b>	<b>7</b>
1.1	Lateral track buckling	7
1.2	Brief review of experimental findings and modelling	8
1.3	Aim and scope	9
<b>2</b>	<b>Constitutive model</b>	<b>10</b>
2.1	Preliminaries	10
2.2	Thermodynamics	11
2.3	Plastic yielding, flow and hardening	12
2.4	Yield surface and plastic potential	12
<b>3</b>	<b>Integration</b>	<b>16</b>
3.1	Incremental relations	16
3.2	Algorithmic tangent stiffness	17
<b>4</b>	<b>Results/model calibration</b>	<b>19</b>
4.1	Lateral ballast resistance tests	20
4.2	Longitudinal ballast resistance tests	23
4.3	Mixed lateral and longitudinal ballast resistance tests	24
<b>5</b>	<b>Discussion and conclusions</b>	<b>29</b>
	<b>References</b>	<b>30</b>
	<b>Appendix A</b>	<b>32</b>
	<b>Appendix B</b>	<b>34</b>

## **Preface**

The work in this report is part in a project that treats various aspects connected with lateral track stability problems and is a joint project between CHARMEC at Chalmers University of Technology and SP and is financially supported by the Swedish National Railway Administration (Banverket). One part of the project concerns methods for force measurements in rails. Another part of the project aims to provide a computational tool in order to be able to analyse various types of CWR tracks and load situations in conjunction with an elevated temperature in the rails.

This report describes a constitutive model that can represent ballast resistance for mixed lateral, longitudinal and vertical loadings. The constitutive model is going to be used in track buckling simulations that will be carried out in a later stage of the project.

## Sammanfattning

En konstitutiv modell baserad på plasticitetsteori med en icke associativ flytlag har utvecklats. Modellen är formulerad i termer av sliperförskjutningar och krafter, och inkluderar hårdnande och mjuknande som styrs av irreversibla transversella (laterala och longitudinella) sliperförskjutningar.

Modellen har kalibrerats med hjälp av resultat från laterala och longitudinella ballastresistansprov (ballast resistance tests). Vidare har resultat från laterala ballastresistansprov med en överlagrad longitudinell kraft för olika vertikala lastnivåer jämförts med experimentella data. Man kan se att det är en bra överensstämmelse mellan resultat från simuleringar och tillgängliga experimentella data.





# 1 Introduction

## 1.1 Lateral track buckling

Lateral buckling of ballasted railway tracks due to the thermal expansion of the rail occurs every summer around the world. This is an old phenomenon, but is unfortunately still present. Modern tracks with continuous welded rail (CWR) are designed to yield, for example, a track allowing for high-speed trains, increased passenger comfort and lowered maintenance costs on the rolling stock, but suffers from the fact that large forces can be build up in the rails due to the thermal expansion in the rails. The annual situations with lateral track buckling cause disturbances in the traffic and bring additional costs to the railway companies due to delays, derailments and extra track maintenance, to mention some of the generated nuisances, and are a problem, cf. [1] and [27]. See also the recent review [13].

A ballasted railway track can be divided into a superstructure and a substructure, cf. [24]. The superstructure contains the rails, sleepers and the fastening system, which attach the rails to the sleepers. Resilient pads are, in addition, placed between the sleepers and the rails to get a soft joint with damping due to the vertical forces induced by the train passages. The substructure is build up in layers with the ballast on top, the subballast in the middle layer and the subgrade. The ballast material is normally chosen as an open graded material consisting of highly angular, crushed high strength rock. For example, the particle sizes are in the range 32–64 mm for Swedish ballast. This yields a material with large internal friction in the ballast material, which is important for the overall track stability. The subballast is ballast of lower quality and the subgrade can be a placed fill material or the existing material depending on the conditions at the actual site.

The sleepers are partly embedded in the ballast material with ballast between the sleepers. Moreover, there is a constructed ballast shoulder on outer sides towards the slopes of the embankment. This design yields an increased resistance against lateral and longitudinal sleeper movements in foundation which is crucial for the track in order to keep its correct position.

The term ballast resistance is often used in lateral track stability context. The ballast resistance can be divided into three types: *lateral*, *longitudinal* and *vertical ballast resistance*, and is the resistance against displacements of a sleeper, decoupled from the rail, subjected to external forces in the lateral, longitudinal and vertical directions, respectively. The resistance against buckling can be split into two main contributors: the superstructure and the ballast resistance. However, the ballast resistance is one of the most important parameters which influences buckling strength, cf. [21] and [22].

The actual ballast resistance depends on a number of parameters such as

- vertical load (the mass of the sleeper and rail, and external loads)
- ballast and sleeper materials
- level of consolidation of the ballast
- sleeper geometry including the design of the sleeper-ballast interface
- the embedding of the sleeper in the ballast including the geometry of the ballast shoulders
- the geometry of the ballast layers

It is noted that all of the items above are more or less fixed except for external loads and the degree of consolidation for an existing track.

A certain degree of consolidation is obtained initially, when a track is constructed or after track maintenance operations. A dynamic track stabilization (DTS) equipment is often used for the compaction (consolidation) operation. The consolidation will, however, increase successively due to repeated loading from the traffic.

The effect of the level of consolidation on the ballast resistance is quite significant. A track with highly consolidated ballast can resist larger lateral and longitudinal forces leading to increased track buckling resistance. Moreover, other effects of high consolidation are that the rate of the accumulation of permanent deformations caused by the repeated load during train passages are less and the elastic stiffness is higher than for poorly consolidated track. The accumulated permanent deformations cause settlements, but also contribute to the track shift, cf. [16] and [17], which affects geometry and thereby also the stability limit for buckling. The railway companies are therefore aiming to obtain as high consolidation as possible in their tracks.

## **1.2 Brief review of experimental findings and modelling**

Experiments in field and in special test setups to explore the ballast resistance have been carried out by several. A number of Single Tie Push Tests (STPT) have been carried out in field in USA by e.g [22] and [23] on a test track site with wooden sleepers and by [25] on a track in operation in order to explore how the lateral ballast resistance is affected by the consolidation. During the STPT, one sleeper is decoupled from its fastening device whereby the sleeper, which is not subjected to any external vertical load, is laterally displaced and the lateral load is registered. In the recent study by [25], the lateral ballast resistance variations in a concrete sleeper track due to surfacing (tamping) and subsequent stabilization/compaction, were investigated. It was found that the peak lateral resistance dropped 43% from 15.1 kN at pre-surfacing to 8.6 kN at post-surfacing. After DTS operation the ballast resistance increased to 11.2 kN. Results on tracks with wooden sleeper in USA cf. [9] and tracks with concrete sleepers in Japan [19] show that a consolidation due to traffic corresponding to 2 MGT yields a lateral peak resistance of 80-85% of the peak resistance prior to a tamping operation. Other results show that 80% of the peak resistance prior to a tamping operation is obtained after 25 MGT traffic, see [18].

Loading tests in three directions were carried out on complete track section with a length of five sleepers at the Roads and the Railway Research Laboratory at TU Delft within the European project ERRI/D202/WG3, cf. [7]. Parts of the results from the tests are also found in [10] and [26] and a summation of the work with conclusions is presented in [11]. The five sleepers were subjected to combinations of different lateral, longitudinal and vertical loads via the rails whereby various ballast resistances were obtained. These experiments are thoroughly described below in the results section.

Results from lateral ballast resistance tests on track sections with varying ballast shoulder height and width have been reported by [4] and [8], cf. [10]. Dogneton [4] found that the peak lateral strength was increased up to 60% by raising the shoulder height but only 5-10% by increasing the shoulder width from 0.65 m to 0.90 m, on for a track with wooden sleepers. Experiments carried out by SNCF [8] included a variation of the sleeper spacing between 0.45 m to 0.65 m, in addition to the variation of the shoulder geometry. They found that the lateral peak resistance decreased when the sleeper spacing was increased. For further information on experimental results, see [9], [10] and [13].

Modelling of ballast resistance has been reported by e.g. [5], [14], [15], [16], [21] and [22] in conjunction with analytical models of the track, and by [1], [6] and [26] used in Finite Element models of the track. The longitudinal and the lateral ballast resistances are usually modelled separately without any coupling. A model with a combined yield criterion, where the lateral and longitudinal responses are dependent on the vertical load, has been proposed by [26], see also [10].

### **1.3 Aim and scope**

The aim of this work is to develop a constitutive model that can be used to represent the ballast resistance in track buckling analyses using a Finite element model for the whole track system. It is important that the constitutive model can resemble the actual ballast resistance for various loading situations that appears during a track buckling situation. Moreover, the model must also be able to be applicable to tracks with different kinds of ballast geometries and consolidation yielding various types of ballast resistances. Similar type of modelling has been presented by [1] and [26], but with simplified constitutive descriptions for the ballast resistance. A user defined element for the Finite element program ABAQUS designed to represent the ballast resistance in a Finite element model has been developed in parallel with the work described in this report, cf. [12].

The report is outlined as follows. The constitutive model, which is within the framework of elasto-plasticity with isotropic hardening and softening, is described in Section 2. The constitutive model is formulated directly in terms of forces and displacements to suite the experimental results. An implicit integration algorithm is used to integrate the slow and hardening laws is outlined in Section 3. Moreover, a general technique to establish the consistent linearized tangent stiffness matrix is presented. A method to calibrate the model using results from lateral and longitudinal ballast resistance tests is outlined in Section 4. Results from model calibrations and predictions are also presented. In Section 5 we summarize and give some conclusions.

## 2 Constitutive model

### 2.1 Preliminaries

This constitutive model describes the ballast resistance, which is defined as the response function obtained when sleepers decoupled from the rail are displaced and the reaction force is measured. More precisely it is the relation between the absolute sleeper displacement  $\mathbf{u}$  (i.e. the sleeper displacement relative a fixed ground) and the resulting forces acting in the sleeper-ballast interface  $\mathbf{F}$  (which is the same as the reaction force in the sleeper when a sleeper decoupled from the rail is displaced).

The definition of  $\mathbf{u}$  and  $\mathbf{F}$  implies that the total response of the subgrade, subballast, ballast and the sleeper-ballast interface are implicitly contained in the model. This means that variations of any of the parts in the embankment regarding material properties or geometry affect the parameter values in the model.

The model should incorporate a yield criterion where plastic deformation caused by transversal (lateral and longitudinal) loading is dependent on the vertical load, cf. the analogy with pressure dependent yield criteria for continuum models. Moreover, plastic dilatancy is present, yielding sleeper (track) uplift during the irreversible transversal deformations and should be part of the model features.

Degrees of freedom in the lateral, longitudinal and the vertical directions relative to the orientation of a railway track are introduced, cf. Figure 1. It is then suitable to define  $\mathbf{u}$  and  $\mathbf{F}$  as following vectors

$$\mathbf{u} = [u_{\text{lat}} \quad u_{\text{long}} \quad u_{\text{vert}}]^T \quad (1)$$

$$\mathbf{F} = [F_{\text{lat}} \quad F_{\text{long}} \quad F_{\text{vert}}]^T \quad (2)$$

where the subscripts *lat*, *long* and *vert* denote components in the lateral, longitudinal and the vertical directions.

It should be noted that variables with boldfaced letters denote vectors and matrices throughout the report.

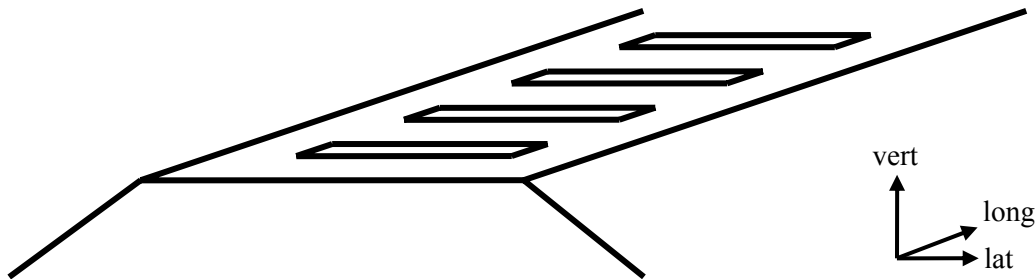


**Figure 1** Schematic picture showing a railway embankment with sleepers and the definition of the degrees of freedom.

## 2.2 Thermodynamics

We shall establish an elastic-plastic model with a yield surface which has a dependency on all three force components with isotropic deformation (cf. strain) hardening and softening. It is noted that the model is thus limited to monotonic loading situations occurring at, e.g. lateral buckling and can not be used in repeated loading situations causing e.g. track-shift cf. [16] and [17].

The thermodynamic state is assumed to be determined by the displacement  $\mathbf{u}$  and the plastic (irreversible) displacement  $\mathbf{u}^p$  which has the initial value  $\mathbf{u}^p(0) = \mathbf{0}$ . Hardening and softening are controlled by a function of the accumulated irreversible displacement  $\mathbf{u}^p$ . Introducing the elastic displacement  $\mathbf{u}^e = \mathbf{u} - \mathbf{u}^p$ , we propose the following expression of the free energy (for a system containing an embankment section with the length of one sleeper)

$$\Psi(\mathbf{u}^e) = \frac{1}{2}(\mathbf{u}^e)^T \mathbf{K} \mathbf{u}^e$$

where  $\mathbf{K}$  is the elastic stiffness matrix

$$\mathbf{K} = \begin{bmatrix} k_{\text{lat}} & 0 & 0 \\ 0 & k_{\text{long}} & 0 \\ 0 & 0 & k_{\text{vert}} \end{bmatrix} \quad (3)$$

with  $k_{\text{lat}}$ ,  $k_{\text{long}}$  and  $k_{\text{vert}}$  denoting the elastic stiffness in respective direction.

The dissipation inequality for this model contains only dissipation from mechanical work and takes the following form

$$D = D_{\text{mech}} = -\dot{\Psi} + \mathbf{F}^T \dot{\mathbf{u}} = \left[ \frac{\partial \Psi}{\partial \mathbf{u}^e} - \mathbf{F} \right]^T \dot{\mathbf{u}}^e + \mathbf{F}^T \dot{\mathbf{u}}^p \geq 0$$

from which we obtain the constitutive relation for  $\mathbf{F}$  as

$$\mathbf{F} = \frac{\partial \Psi}{\partial \mathbf{u}^e} = \mathbf{K} \mathbf{u}^e \quad (4)$$

This yields the reduced dissipation inequality

$$D = \mathbf{F}^T \dot{\mathbf{u}}^p \geq 0 \quad (5)$$

which is shown to be fulfilled for this model when no hardening or softening is present, see Appendix A.

**Remark:** Additional terms will enter into the dissipation inequality due to hardening and softening. The explicit expressions for the dissipation have not yet been derived for those cases. <sup>1</sup>

## 2.3 Plastic yielding, flow and hardening

It is assumed that the ballast materials in the track are consolidated to a certain level and that no additional (plastic) consolidation takes place due to vertical loading. Further, it is assumed that the hardening and softening are controlled by the amount of irreversible deformations in the transversal (lateral and longitudinal) directions. We therefore introduce the hardening variable  $\kappa$  with following rate law

$$\dot{\kappa} = \left[ (\dot{u}_{\text{lat}}^{\text{p}})^2 + (\dot{u}_{\text{long}}^{\text{p}})^2 \right]^{\frac{1}{2}} \quad (6)$$

where the superimposed dot denotes *time derivative*, i.e.

$$(\dot{\bullet}) \stackrel{\text{def}}{=} \frac{d(\bullet)}{dt}$$

The convex set of admissible forces  $\mathbf{F}$  for a given value of  $\kappa$  is defined as

$$B(\kappa) = \{ \mathbf{F} \mid \phi(\mathbf{F}; \kappa) \leq 0 \}$$

where  $\phi(\mathbf{F}; \kappa) = 0$  is the convex yield surface for given  $\kappa$ . The evolution law for plastic displacements is chosen as

$$\dot{\mathbf{u}}^{\text{p}} = \mu \mathbf{f}^* \quad \text{with} \quad \mathbf{f}^* \stackrel{\text{def}}{=} \frac{\partial \phi^*}{\partial \mathbf{F}} \quad (7)$$

where  $\phi^*(\mathbf{F}) = 0$  is a flow potential. The flow rule for the plastic deformations is non-associative as  $\phi^* \neq \phi$ . The plastic multiplier  $\mu$  is determined by the Karush-Kuhn-Tucker loading conditions

$$\mu \geq 0, \quad \phi(\mathbf{F}; \kappa) \leq 0, \quad \mu \phi(\mathbf{F}; \kappa) = 0 \quad (8)$$

The complete set of constitutive equations are defined by the state equation for  $\mathbf{F}$  in (4) and by the rate laws for  $\kappa$  and  $\mathbf{u}^{\text{p}}$  in (6) and (7), and by the loading conditions (8).

## 2.4 Yield surface and plastic potential

### Yield surface

Experimental results from [7] ([10] and [26]) show that the ballast resistance is dependent on the vertical load. It is found that the magnitude of the transversal (lateral and longitudinal) ballast resistance is approximately linearly dependent on the magnitude of the vertical force implying a constant friction coefficient for transversal loading. However, the experiments show that the longitudinal ballast resistance is slightly higher than for the lateral ballast resistance at the same vertical force level.

Guided by the experimental results described above together with additional experimental data from [7] ([10] and [26]) on combined loading situations lead us to the position to introduce the yield function  $\phi$  defined in the vectorial space of forces as follows:

$$\phi(\mathbf{F}; \kappa) = F_{\text{c}} + M(\kappa)[F_{\text{vert}} - F_{\text{c}}] + c \quad (9)$$

where

$$F_e = \left[ (F_{\text{lat}})^2 + (aF_{\text{long}})^2 \right]^{\frac{1}{2}} \quad (10)$$

can be viewed as an effective transversal force, in which  $a$  is a weight (or shape) parameter controlling the impact of  $F_{\text{long}}$  in the effective transversal force  $F_e$ . The parameter  $M$  determines the transversal friction and is defined as

$$M(\kappa) = \begin{cases} M_i + (M_p - M_i) \left[ 1 - (1 - \kappa/\kappa_p)^n \right], & (0 \leq \kappa/\kappa_p \leq 1) \\ M_p - (M_p - M_f) \frac{H(\kappa/\kappa_p - 1)}{M_p - M_f + H(\kappa/\kappa_p - 1)}, & (\kappa/\kappa_p > 1) \end{cases} \quad (11)$$

where  $M_i$ ,  $M_p$  and  $M_f$  are the values of  $M$ , initially ( $\kappa = 0$ ), at peak ( $\kappa/\kappa_p = 1$ ), and at failure ( $\kappa \rightarrow \infty$ ), respectively. Furthermore, the parameter  $\kappa_p$  represents the value of  $\kappa$  at peak. Moreover,  $n$  and  $H$  are parameters that control the hardening and softening behaviour, respectively. Finally,  $F_c$  and  $c$  (together with  $M$ ) are parameters yielding the amount of cohesion and the position of the apex of the yield surface, i.e. when  $F_{\text{lat}} = F_{\text{long}} = 0$ . The yield surface, which bears a resemblance to the Drucker-Prager yield function, is visualized in Figure 2. It is noted that the position of the apex of the yield surface at  $F_e = 0$ , given as

$$F_{\text{vert}}^{\text{apex}}(\kappa) = F_c - c/M(\kappa), \quad (12)$$

changes due to hardening and softening, cf. Figure 2.

**Remark:** Another feasible choice of yield function would e.g. be

$$\phi(\mathbf{F}; \kappa) = F_e + M(\kappa)F_{\text{vert}} - c \quad (13)$$

in which the position of the apex is constant. This choice of function has one parameter less than (9). However, in the form the experimental data are given, cf. Section 4.1, it will

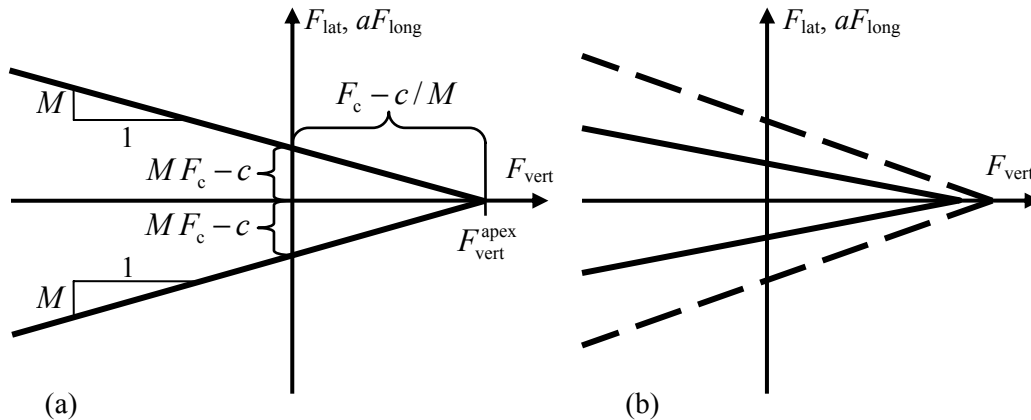


**Figure 2** Yield surface  $\phi = 0$  in meridian plane; (a) Visualization of the various parameters; (b) Peak (dashed lines) and failure (solid lines) states.

turn out that the part of the calibration procedure when suitable values for  $M_p$  and  $M_f$  are to be determined, in fact, is simpler with the choice (9) compared with using (13).<sup>†</sup>

### Plastic potential

The plastic potential surface  $\phi^*(\mathbf{F}) = 0$ , depicted in Figure 3, is chosen as

$$\phi^*(\mathbf{F}) = \frac{(F_e^*)^2 - (M^*)^2 \left[ (F_c^* - F_{\text{vert}} + F_0)^2 - F_0^2 \right]}{k_{\text{vert}}} \quad (14)$$

where  $F_e^*$  is defined as

$$F_e^* = \left[ (F_{\text{lat}})^2 + (a^* F_{\text{long}})^2 \right]^{\frac{1}{2}} \quad (15)$$

and where  $a^*$  is a shape parameter for the flow potential in the  $F_{\text{lat}} - F_{\text{long}}$ -plane, i.e. the plane of transversal forces, in the space of forces (cf. the deviatoric stress plane in stress space), see Figure 3(a). The parameter  $a^*$  yields a non-associativity in the flow rule and is explicitly controlling the magnitude of  $\dot{u}_{\text{long}}^p$  in the flow rule. The case when  $a^* = a$  implies an associative flow rule in the plane of transversal forces, which would be visualized as a circular shaped surface in the plane of transversal forces, cf. Figure 3(a).

The parameter  $M^*$  is controlling the amount of plastic dilatancy (i.e. vertical plastic deformations yielding an uplift of the sleepers) and  $F_0$  is a parameter that defines the size of the curvature of the potential surface in the meridian plane, see Figure 3(b). The parameter  $k_{\text{vert}}$  is only introduced as a scaling parameter for numerical reasons when the constitutive equations are solved.

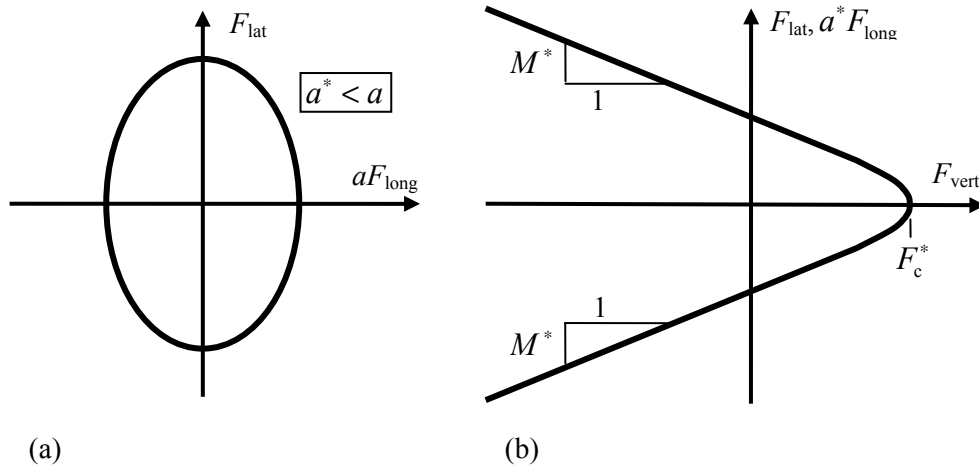


**Figure 3** Plastic potential surface  $\phi^* = 0$ ; (a) Plane of transversal forces, in the space of forces, when  $a^* < a$ ; (b) Meridian force plane.



Moreover,  $\phi^*(\mathbf{F}) = 0$  holds at plastic yielding, which implies that  $F_c^*$  can be solved for in (y5) which gives

$$F_c^*(\mathbf{F}) = F_{\text{vert}} - F_0 + \sqrt{\left(\frac{F_e^*}{M^*}\right)^2 + F_0^2} \quad (16)$$

**Remark:** It is seen that the surface has a curved shape in the meridian plane, with a gradient pointing in the direction along the  $F_{\text{vert}}$ -axis when  $F_c^* = 0$ , cf. Figure 3. The special numerical treatment that is necessary with potential surfaces having an apex, when the integrated constitutive equations are solved, is thus avoided, cf. e.g. [3]. However, the potential surface  $\phi^*(\mathbf{F}) = 0$  approaches a Drucker-Prager shaped surface in the limit when  $F_0 \rightarrow 0$ , which has an apex. <sup>1</sup>

Next, we introduce the gradients of  $\phi^*$  with respect to  $\mathbf{F}$  as

$$f_{\text{lat}}^* \stackrel{\text{def}}{=} \frac{\partial \phi^*}{\partial F_{\text{lat}}}, \quad f_{\text{long}}^* \stackrel{\text{def}}{=} \frac{\partial \phi^*}{\partial F_{\text{long}}} \quad \text{and} \quad f_{\text{vert}}^* \stackrel{\text{def}}{=} \frac{\partial \phi^*}{\partial F_{\text{vert}}} \quad (17\text{a-c})$$

where the pertinent derivations are found in Appendix B.

**Remark:** The parameter  $F_c^*$  must be considered as a constant when the gradients of  $\phi^*$  are evaluated for a fixed force state  $\mathbf{F}$ . However, when a consistent linearization of the incremental relations is computed, then  $F_c^*(\mathbf{F})$  must be considered as a function of the stress state, cf. below. <sup>1</sup>

With the definitions in (7) and (17a-b), we restate the rate law for  $\kappa$  in (6) as

$$\dot{\kappa} = \mu f_{\kappa}^* \quad \text{with} \quad f_{\kappa}^* \stackrel{\text{def}}{=} \left[ (f_{\text{lat}}^*)^2 + (f_{\text{long}}^*)^2 \right]^{1/2} \quad (18)$$

### 3 Integration

#### 3.1 Incremental relations

We start by discretizing the time considered time interval  $T$  into  $N$  increments as follows:

$$[0, T] = \bigcup_{n=0}^{N-1} {}^{n+1}(\Delta t), \quad {}^{n+1}(\Delta t) = {}^{n+1}t - {}^n t, \quad {}^0 t = 0$$

Applying the fully implicit (Backward Euler) integration rule for integrating the evolution equations (7) and (18) we obtain

$${}^{n+1} \mathbf{u}^p = {}^n \mathbf{u}^p + \Delta \mu {}^{n+1} \mathbf{f}^* \quad (19)$$

$$\boldsymbol{\kappa} = {}^n \boldsymbol{\kappa} + \Delta \mu f_{\boldsymbol{\kappa}}^* \quad (20)$$

By recalling that  ${}^{n+1} \mathbf{u}^e = {}^{n+1} \mathbf{u} - {}^{n+1} \mathbf{u}^p$  we rewrite (19) as

$${}^{n+1} \mathbf{u}^e = {}^{n+1} \mathbf{u}^{e, \text{tr}} - \Delta \mu {}^{n+1} \mathbf{f}^* \quad (21)$$

where

$${}^{n+1} \mathbf{u}^{e, \text{tr}} = {}^{n+1} \mathbf{u} - {}^n \mathbf{u}^p \quad (22)$$

The discrete form of the loading conditions (8) becomes

$$\Delta \mu \geq 0, \quad \phi({}^{n+1} \mathbf{F}; {}^{n+1} \boldsymbol{\kappa}) \leq 0, \quad \Delta \mu \phi({}^{n+1} \mathbf{F}; {}^{n+1} \boldsymbol{\kappa}) = 0 \quad (23)$$

Hence, (20), (21), (23) together with (4) completely define the solution of the incrementally non-linear problem in terms of the unknowns  ${}^{n+1} \mathbf{u}^e$  and  ${}^{n+1} \boldsymbol{\kappa}$  (for given  ${}^{n+1} \mathbf{u}$ ) before the next time step is taken. We will subsequently omit the superindex  $n+1$ , referring to time  ${}^{n+1}t$ , in order to abbreviate the notation.

By rewriting (21) by means of (17a-c) we obtain following set of equations

$$\begin{aligned} u_{\text{lat}}^e &= u_{\text{lat}}^{e, \text{tr}} - \Delta \mu f_{\text{lat}}^* \\ u_{\text{long}}^e &= u_{\text{long}}^{e, \text{tr}} - \Delta \mu f_{\text{long}}^* \\ u_{\text{vert}}^e &= u_{\text{vert}}^{e, \text{tr}} - \Delta \mu f_{\text{vert}}^* \end{aligned} \quad (24 \text{ a-c})$$

together with

$$\boldsymbol{\kappa} = {}^n \boldsymbol{\kappa} + \Delta \mu f_{\boldsymbol{\kappa}}^* \quad (25)$$

with loading the conditions

$$\Delta \mu \geq 0, \quad \phi(F_{\text{lat}}, F_{\text{long}}, F_{\text{vert}}; \boldsymbol{\kappa}) \leq 0, \quad \Delta \mu \phi(F_{\text{lat}}, F_{\text{long}}, F_{\text{vert}}; \boldsymbol{\kappa}) = 0$$

The system (24a-c) is conveniently solved for  $u_{\text{lat}}^e$ ,  $u_{\text{long}}^e$  and  $u_{\text{vert}}^e$  using a Newton procedure. The appropriate relations in a formal setting are then obtained from (24a-c) as

$$\begin{aligned}
Y_{u_{\text{lat}}^e} (u_{\text{lat}}^e, \Delta\mu) &= u_{\text{lat}}^e - u_{\text{lat}}^{e,\text{tr}} + \Delta\mu f_{\text{lat}}^* (u_{\text{lat}}^e) = 0 \\
Y_{u_{\text{long}}^e} (u_{\text{long}}^e, \Delta\mu) &= u_{\text{long}}^e - u_{\text{long}}^{e,\text{tr}} + \Delta\mu f_{\text{long}}^* (u_{\text{long}}^e) = 0 \\
Y_{u_{\text{vert}}^e} (u_{\text{lat}}^e, u_{\text{long}}^e, u_{\text{vert}}^e, \Delta\mu) &= u_{\text{vert}}^e - u_{\text{vert}}^{e,\text{tr}} + \Delta\mu f_{\text{vert}}^* (u_{\text{lat}}^e, u_{\text{long}}^e) = 0 \\
Y_{\phi} (u_{\text{lat}}^e, u_{\text{long}}^e, u_{\text{vert}}^e, \Delta\mu) &= \phi(u_{\text{lat}}^e, u_{\text{long}}^e, u_{\text{vert}}^e, \Delta\mu) / k_{\text{vert}} = 0
\end{aligned} \tag{26a-d}$$

The set of equations (26a) to (26d) is summarized in matrix form as

$$\mathbf{Y}(\mathbf{X}) = \mathbf{0} \quad \text{with} \quad \mathbf{Y} = \begin{bmatrix} Y_{u_{\text{lat}}^e} & Y_{u_{\text{long}}^e} & Y_{u_{\text{vert}}^e} & Y_{\phi} \end{bmatrix}^T \quad \text{and} \quad \mathbf{X} = \begin{bmatrix} u_{\text{lat}}^e & u_{\text{long}}^e & u_{\text{vert}}^e & \Delta\mu \end{bmatrix}^T \tag{27}$$

The Jacobian of  $\mathbf{Y}$ , which is needed to carry out the Newton iterations on (27) is given as

$$\mathbf{J} \stackrel{\text{def}}{=} \frac{d\mathbf{Y}}{d\mathbf{X}} = \begin{bmatrix} 1 + \Delta\mu \frac{df_{\text{lat}}^*}{du_{\text{lat}}^e} & 0 & 0 & f_{\text{lat}}^* \\ 0 & 1 + \Delta\mu \frac{df_{\text{long}}^*}{du_{\text{long}}^e} & 0 & f_{\text{long}}^* \\ \Delta\mu \frac{df_{\text{vert}}^*}{du_{\text{lat}}^e} & \Delta\mu \frac{df_{\text{vert}}^*}{du_{\text{long}}^e} & 1 & f_{\text{vert}}^* \\ \frac{1}{k_{\text{vert}}} \frac{d\phi}{du_{\text{lat}}^e} & \frac{1}{k_{\text{vert}}} \frac{d\phi}{du_{\text{long}}^e} & \frac{1}{k_{\text{vert}}} \frac{d\phi}{du_{\text{vert}}^e} & \frac{1}{k_{\text{vert}}} \frac{d\phi}{d\Delta\mu} \end{bmatrix} \tag{28}$$

in which additional derivations for terms in (28) are found in Appendix B.

## 3.2 Algorithmic tangent stiffness

The ATS-matrix, or consistent tangent stiffness matrix,  $\mathbf{K}_a$ , is required to achieve quadratic convergence rate at equilibrium iterations that aim at satisfying the prescribed force condition under mixed control. Moreover, in conjunction with finite-element computations,  $\mathbf{K}_a$ , is used for equilibrium iterations within displacement formulated format. The ATS-matrix is defined as

$$d(\Delta\mathbf{F}) = \mathbf{K}_a d(\Delta\mathbf{u}) \tag{29}$$

where it was used that  $\mathbf{F}(\Delta\mathbf{u}) = {}^n\mathbf{F} + \Delta\mathbf{F}(\Delta\mathbf{u})$  in a displacement-driven integration algorithm. We know that

$$\mathbf{F}(\Delta\mathbf{u}) = \mathbf{F}(\mathbf{X}(\Delta\mathbf{u})) = \mathbf{K} \mathbf{u}^e(\Delta\mathbf{u}) \tag{30}$$

By differentiation of (29) we obtain

$$\mathbf{K}_a = \frac{d(\Delta\mathbf{F})}{d(\Delta\mathbf{u})} = \frac{d\mathbf{F}(\Delta\mathbf{u})}{d(\Delta\mathbf{u})} = \frac{\partial\mathbf{F}}{\partial\mathbf{X}} \frac{d\mathbf{X}}{d(\Delta\mathbf{u})} = \mathbf{K}\mathbf{A}^T \frac{d\mathbf{X}}{d(\Delta\mathbf{u})} \quad (31)$$

where

$$\frac{\partial\mathbf{F}}{\partial\mathbf{X}} = \frac{\partial\mathbf{F}}{\partial\mathbf{u}^e} \frac{\partial\mathbf{u}^e}{\partial\mathbf{X}}$$

was used and where

$$\mathbf{A}^T \stackrel{\text{def}}{=} \frac{\partial\mathbf{u}^e}{\partial\mathbf{X}} = [\mathbf{I} \quad \mathbf{0}]$$

in which  $\mathbf{I}$  denotes the (3x3) identity matrix and  $\mathbf{0}$  denotes a (3x1) vector with zeros.

In order to obtain  $d\mathbf{X}/d(\Delta\mathbf{u})$  we assume plastic loading and reconsider the local system of equations (27) reformulated as

$$\mathbf{Y}(\mathbf{X}(\Delta\mathbf{u}), \Delta\mathbf{u}) = \mathbf{0} \quad (32)$$

Differentiating (32) yields

$$d\mathbf{Y} = \frac{\partial\mathbf{Y}}{\partial\mathbf{X}} \frac{d\mathbf{X}}{d(\Delta\mathbf{u})} + \frac{\partial\mathbf{Y}}{\partial(\Delta\mathbf{u})} = \mathbf{0} \quad (33)$$

from which we obtain

$$\frac{d\mathbf{X}}{d(\Delta\mathbf{u})} = -\mathbf{J}^{-1} \frac{\partial\mathbf{Y}}{\partial(\Delta\mathbf{u})} \quad (34)$$

where the Jacobian,  $\mathbf{J}$ , was recognized from (28). From (26a-d) follows

$$\frac{\partial\mathbf{Y}}{\partial(\Delta\mathbf{u})} = \begin{bmatrix} -\mathbf{I} \\ \mathbf{0}^T \end{bmatrix} = -\mathbf{A} \quad (35)$$

where the relation  $d(\Delta\mathbf{u}) = d\mathbf{u}$  was used. By inserting (34) and (35) in (31) yields finally

$$\mathbf{K}_a = \mathbf{K}(\mathbf{A}^T \mathbf{J}^{-1} \mathbf{A}) \quad (36)$$

It is noted that  $\mathbf{K}_a$  is non-symmetric, which is due to the non-associative flow rule.

## 4 Results/model calibration

The constitutive model is calibrated using results from ballast resistance tests carried out at the Roads and the Railway Research Laboratory at TU Delft within the European project ERRI/D202/WG3, cf. [7] and [10]. Results from the tests are also reported in [26]. A track section containing ballast, sleepers, fastenings, pads and rails, with a length corresponding to five sleepers, was built up in the laboratory. The superstructure consisting of the sleepers interconnected by the rails were displaced as one unit in the tests. This test setup differs from the STPT that has been carried out in field in e.g USA cf. [22], [23] and [25], in which only one sleeper is (laterally) displaced. Furthermore, the ballast was tamped and compacted manually yielding a track section with moderate consolidation corresponding to a weak track according to the terminology used by e.g. Samavedam and co-workers [22] and [23].

Ballast resistance tests, in which the superstructure was transversally displaced, were carried out for a number of different constant vertical load levels. Various number of concrete slabs piled on the track were used to accomplish the different constant vertical loads. A number of tests was carried out with only the dead weight (d.w.) of the sleepers, fastenings and rails that were part of the test setup, which in total constitutes to a vertical force of  $F_{\text{vert}}^{\text{d.w.}} = -3.6$  kN per sleeper. Moreover, tests in which an uplift force accomplished by a crane, were also conducted. In total eight different applied constant vertical load levels  $F_{\text{vert}}^{\text{ext}}$  were used, which are listed in Table 1. The total force on the embankment (per sleeper),  $F_{\text{vert}}$ , is thus given as

$$F_{\text{vert}} = F_{\text{vert}}^{\text{ext}} + F_{\text{vert}}^{\text{d.w.}} \quad (37)$$

An uplift force was applied at the two highest vertical load levels (7 and 8). The uplift force at the highest load level, i.e.  $F_{\text{vert}}^{\text{ext}} = 4$  kN, was slightly exceeding  $F_{\text{vert}}^{\text{d.w.}}$ , yielding approximately a zero net loading on the embankment. The largest downward force, i.e.  $F_{\text{vert}}^{\text{ext}} = -31.8$  kN, corresponds to an axle load of a light train.

Three types of tests were carried out:

- (a) lateral ballast resistance tests with  $0 \leq u_{\text{lat}} \leq 0.2$  m and  $F_{\text{long}} = 0$  kN
- (b) longitudinal ballast resistance tests with  $F_{\text{lat}} = 0$  kN and  $0 \leq u_{\text{long}} \leq 0.05$  m
- (c) lateral ballast resistance tests with a superimposed constant longitudinal load, i.e.  $0 \leq u_{\text{lat}} \leq 0.2$  m and  $F_{\text{long}} = \text{constant} > 0$  kN

in which the reaction forces were measured. Furthermore, the displacement rate was 10 mm/min in all tests.

**Table 1 Vertical applied vertical load levels in the ballast resistance tests.**

Load level	1	2	3	4	5	6	7	8
$F_{\text{vert}}^{\text{ext}}$ [kN]	-31.8	-15.9	-11.9	-8	-4	0	2	4

Results from lateral ballast resistance tests (type a) and model calibration are shown in Section 4.1. Longitudinal ballast resistance tests (type b) together with model calibration and predictions are shown in Section 4.2. Predicted results together with results from experiments from lateral ballast resistance tests with superimposed longitudinal loading (type c) are shown in Section 4.3.

## 4.1 Lateral ballast resistance tests

Results from lateral ballast resistance tests (type a), with eight different applied constant vertical loads  $F_{\text{vert}}^{\text{ext}}$ , cf. Table 1, were reported. The lateral peak load and the load after 0.2 m lateral displacement were recorded. We will subsequently denote the latter state as *quasi failure*. (The notation quasi is added to distinguish from the theoretical failure state in which the transversal displacement approaches infinity.) It was found that both the peak loads and the loads at quasi failure displayed a linear relationship with the vertical load, with increasing lateral resistance for an increasing load downwards, yielding

$$F_{\text{lat,p}} = -m_p F_{\text{vert}} + c_p \quad \text{with } m_p = 0.7247 \text{ and } c_p = 6.40 \text{ [kN]} \quad (38)$$

$$F_{\text{lat,\bar{f}}} = -m_{\bar{f}} F_{\text{vert}} + c_{\bar{f}} \quad \text{with } m_{\bar{f}} = 0.6561 \text{ and } c_{\bar{f}} = 5.31 \text{ [kN]} \quad (39)$$

where the subscripts “p” and “ $\bar{f}$ ” stand for the *peak* and *quasi failure* states. Moreover,  $F_{\text{vert}}$  is the *total vertical force* acting on the embankment (per sleeper distance), according to (37). The coefficients  $m_p$  and  $m_{\bar{f}}$  may be viewed as friction numbers (coefficients), and the parameters  $c_p$  and  $c_{\bar{f}}$  represent the apparent cohesion.

At the lateral peak load and at quasi failure it follows from (9) and (11) that

$$F_{\text{lat,p}} = -M_p F_{\text{vert}} + M_p F_c - c \quad (40)$$

$$F_{\text{lat,\bar{f}}} = -M_{\bar{f}} F_{\text{vert}} + M_{\bar{f}} F_c - c \quad (41)$$

where  $M_{\bar{f}} \stackrel{\text{def}}{=} M(\kappa_{\bar{f}})$  and  $\kappa_{\bar{f}}$  is the value of  $\kappa$  at quasi failure. By comparing (38) and (40), and (39) and (41), we conclude that

$$M_p = m_p \quad \text{and} \quad M_p F_c - c = c_p \quad (42a,b)$$

$$M_{\bar{f}} = m_{\bar{f}} \quad \text{and} \quad M_{\bar{f}} F_c - c = c_{\bar{f}} \quad (43a,b)$$

Solving for  $F_c$  and  $c$  from (42b) and (43b) and using the results (42a) and (43a) yields

$$F_c = \frac{c_p - c_{\bar{f}}}{M_p - M_{\bar{f}}} = \frac{c_p - c_{\bar{f}}}{m_p - m_{\bar{f}}} \quad (44)$$

$$c = \frac{M_{\bar{f}} c_p - M_p c_{\bar{f}}}{M_p - M_{\bar{f}}} = \frac{m_{\bar{f}} c_p - m_p c_{\bar{f}}}{m_p - m_{\bar{f}}} \quad (45)$$

From (42a) and (43a) and the definition of  $M_{\bar{f}}$  follows

$$m_{\bar{f}} = M_{\bar{f}} = M_p - (M_p - M_f) \frac{K}{M_p - M_f + K} = m_p - (m_p - M_f) \frac{K}{m_p - M_f + K} \quad (46)$$

where  $K = H(\kappa_{\bar{f}} / \kappa_p - 1)$ . Solving for  $M_f$  in (46) yields

$$M_f = \frac{m_p^2 - m_{\bar{f}}K - m_{\bar{f}}m_p}{m_p - m_{\bar{f}} - K} \quad (47)$$

We conclude from (6) that  $\kappa = u_{\text{lat}}^p$  in the lateral ballast resistance tests. Moreover, the plastic deformation constitutes a large part of the total deformation, except for the very first part of the loading. It is thus reasonable to assume that  $u_{\text{lat}} \approx u_{\text{lat}}^p$  at peak and quasi failure. Hence, we assume that  $\kappa_p \approx u_{\text{lat,p}}$  and  $\kappa_{\bar{f}} \approx u_{\text{lat,\bar{f}}} = 0.2$  m. Experimental data show that the lateral deformation at peak  $u_{\text{lat,p}}$  was estimated to be in the range between 0.020–0.085 m, with the main part of the results lying around 0.030–0.045 m, cf. Figure 9.

Force-deformation relations obtained from lateral ballast resistance tests [7] were used to determine the elastic stiffness  $k_{\text{lat}}$ , the initial size of the yield surface  $M_i$ , the parameters  $n$ ,  $H$  and  $\kappa_p$  in the hardening/softening law. Results on the vertical versus lateral displacement at quasi failure were also reported by [7]. The results are, however, hard to interpret and the vertical displacement was estimated to be around 7 mm when  $F_{\text{vert}}^{\text{ext}} = -31.9$  kN and around 20 mm when  $F_{\text{vert}}^{\text{ext}} = -4$  kN, when  $u_{\text{lat}} = 0.2$  m. These values have to be considered as rough estimates and were used to determine the parameters  $M^*$  and  $F_0$ , that control the vertical plastic deformations (plastic dilatancy).

In order to find a appropriate value for the vertical elastic stiffness  $k_{\text{vert}}$ , we resort to other results. Results from field measurements in Sweden cf. [20], revealed that the vertical elastic secant stiffness was in the range between 75–260 MN/m for a particular track section. It was also found that the stiffness could vary significantly between adjacent sleepers. Moreover, the response is non-linear, which is not accounted for in this version of the constitutive model.

Results from simulations and experiments from lateral ballast resistance tests for five vertical load levels are shown in Figures 4 and 5. The lateral force versus lateral displacement obtained from simulations and experiments are shown in Figure 4. The force at peak and at quasi failure according to (38) and (39) are, in addition, shown in Figure 4. The graph shows that the calibration procedure in order to set the parameters for the yield surface defining the lateral force at peak and at quasi failure works. The vertical versus lateral displacement is shown in Figure 5.

A summary of parameter values is listed in Table 2 in Section 4.2.

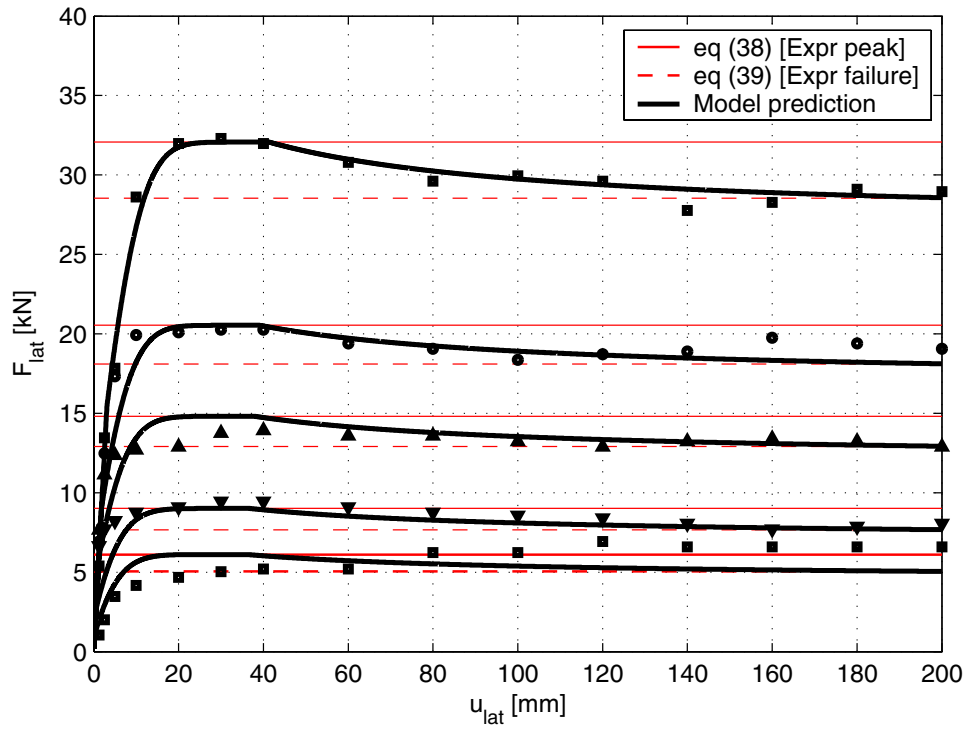


**Figure 4** Simulated response from lateral ballast resistance tests (black curves) for five vertical loads,  $F_{\text{vert}}^{\text{ext}} = \{-31.8, -15.9, -8, 0, 4\}$  [kN], together with pertinent levels for lateral resistance at peak (red solid lines) and at quasi failure (red dashed lines) according to the experimentally based equations (38) and (39). The markers denote experimental results from [7].

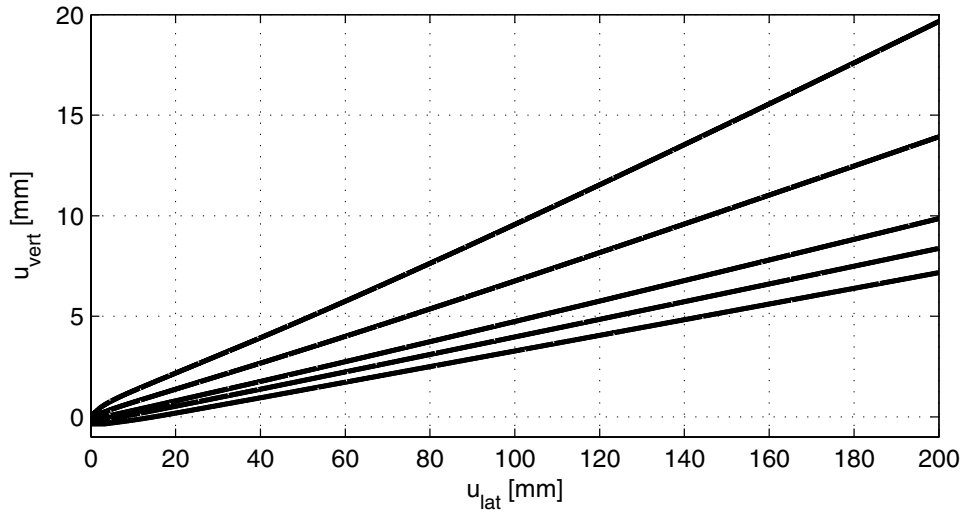


**Figure 5** Simulated response from lateral ballast resistance tests for five vertical loads,  $F_{\text{vert}}^{\text{ext}} = \{-31.8, -15.9, -8, 0, 4\}$  [kN]. The lowest and the uppermost curves correspond to  $F_{\text{vert}}^{\text{ext}} = -31.9$  [kN] and  $F_{\text{vert}}^{\text{ext}} = 4$  [kN], respectively.



## 4.2 Longitudinal ballast resistance tests

Longitudinal ballast resistance tests (type b) carried out with eight different applied constant vertical loads were reported by [7], ([10], [26]). The vertical load levels  $F_{\text{vert}}^{\text{ext}}$  are listed in Table 1. It was revealed that slippage between the rails and the sleepers occurred in the fastening system, i.e. the peak longitudinal ballast resistance was higher than the longitudinal resistance in the fastening system, at the tests with the two highest downward vertical loads (load levels 1 and 2 in Table 1). The range of vertical loads yielding peak longitudinal forces suitable model calibration are thus those of load levels 3 to 8 listed in Table 1.

The peak values of the longitudinal force obtained at the longitudinal ballast resistance tests,  $F_{\text{long,p}}(F_{\text{vert},i}^{\text{ext}})$ , where  $F_{\text{vert},i}^{\text{ext}}$ ,  $i = 3, \dots, 8$ , corresponding to load levels 3 to 8, will be used to determine  $a$ , which is the remaining parameter in the yield function to be set. According to the expressions for the yield function (9) and (10) at maximum hardening (at peak) given by  $\kappa / \kappa_p = 1$ , it follows that

$$F_{\text{lat,p}}(F_{\text{vert}}) = aF_{\text{long,p}}(F_{\text{vert}}) \quad (48)$$

for a given vertical force  $F_{\text{vert}}$ . The parameter  $a$  can be determined by forming an optimization problem by minimizing an objective function  $E(a)$ , which quantifies the error between the model values and experimental data, by varying  $a$ . We may formally state the problem as: Find the optimal solution  $a_{\text{opt}}$

$$a_{\text{opt}} = \arg[\min_{a>0} E(a)] \quad (49)$$

where

$$E = \left\{ \sum_{i=3}^8 [F_{\text{lat,p}}(F_{\text{vert},i}^{\text{ext}}) - aF_{\text{long,p}}(F_{\text{vert},i}^{\text{ext}})]^2 \right\}^{1/2} \quad (50)$$

in which the relations (38) and (48) were used. By carrying out (49) we get  $a_{\text{opt}} = 0.858$ .

A complete list of all parameter used in the simulations is found in Table 2. Results from simulations and experiments are shown in Figure 6.

**Table 2 Parameter values for the constitutive model.**

	Elasticity	Plastic yielding		Hardening/ softening		Plastic flow	
$k_{\text{lat}}$	5.0 [MN/m]	$M_i$	0.40	$H$	0.05	$a^* / a$	0.7
$k_{\text{long}}$	3.5 [MN/m]	$M_p$	0.725	$n$	8.0	$M^*$	0.035
$k_{\text{vert}}$	100 [MN/m]	$M_f$	0.627	$\kappa_p$	0.035 [m]	$F_0$	400 [kN]
		$F_c$	15.8 [kN]				
		$c$	5.07 [kN]				
		$a$	0.858				

### 4.3 Mixed lateral and longitudinal ballast resistance tests

Simulations of lateral ballast resistance tests (type c) with a superimposed constant prescribed longitudinal load  $F_{\text{long}}^{\text{pre}}$ , with different applied constant vertical loads  $F_{\text{vert}}^{\text{ext}}$  have been carried out using the parameter values determined in Sections 4.1 and 4.2. The load steps during the test are (1) applying the prescribed vertical load, (2) applying the prescribed longitudinal load and (3) applying a lateral displacement  $u_{\text{lat}}$  from  $u_{\text{lat}} = 0$  m to  $u_{\text{lat}} = u_{\text{lat},\bar{f}}$  where  $u_{\text{lat},\bar{f}} = 0.050$  m.

There is an upper limit on prescribed longitudinal force  $F_{\text{long}}^{\text{pre}}$  that can be used without causing failure before the prescribed final lateral displacement is reached, which subsequently will be denoted  $F_{\text{long,max}}^{\text{pre}}$ . This upper limit can be approximated by the value of  $F_{\text{long}}$  at failure obtained from pure longitudinal ballast resistance tests (type b), i.e.

$$F_{\text{long},f} = \frac{1}{a} [-M_f (F_{\text{vert}} - F_c) - c] \quad (51)$$

obtained from (9) and (10). However, the theoretical failure state (full softening) is not reached in the mixed loading tests. This means that (51) is a conservative estimate. By numerical experiments a better estimate of  $F_{\text{long,max}}^{\text{pre}}$  is found as

$$F_{\text{long,max}}^{\text{pre}} = C \cdot F_{\text{long},\bar{f}} \quad (52)$$

where  $F_{\text{long},\bar{f}}$  is the value of  $F_{\text{long}}$  at quasi-failure and where the constant  $C \approx 0.80$  was

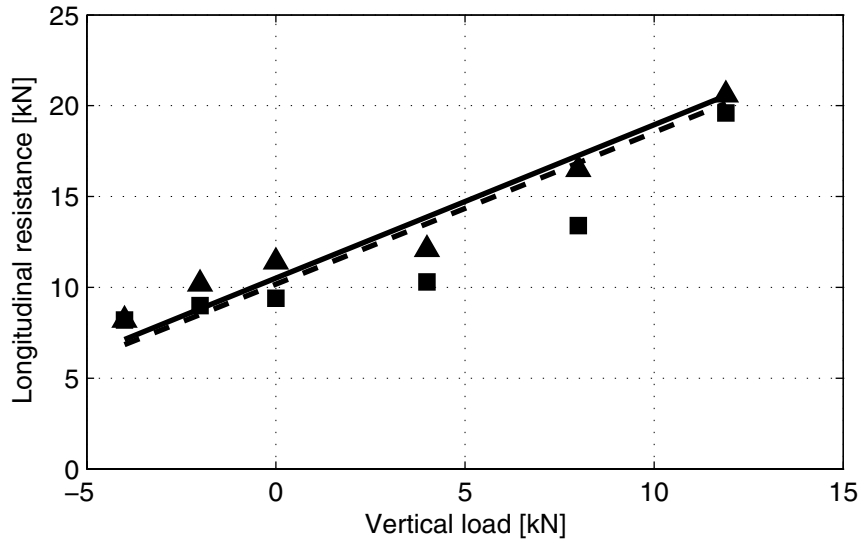


**Figure 6** Longitudinal ballast resistance at peak and at quasi failure. The solid line and triangular markers denote results at peak from computations and experiments, respectively, and were used in the calibration. The dashed line and square markers denote results at quasi failure from predictions and experiments, respectively.

numerically determined. A number of simulations of the mixed loading tests (type c) with different vertical loads and with prescribed longitudinal loads  $F_{\text{long},i}^{\text{pre}}$  according to

$$F_{\text{long},i}^{\text{pre}} = \alpha_i F_{\text{long,max}}^{\text{pre}} \text{ with } \alpha_i = i/10 \text{ where } i = 0, 1, \dots, 10$$

and with  $F_{\text{long,max}}^{\text{pre}}$  given by (52), have been carried out.

The peak lateral ballast resistances and the resistances at quasi failure are summarized in Figures 7 and 8. Moreover, the longitudinal resistance values at peak and at quasi failure, cf. Section 4.2, are also visualized in the Figures 7 and 8 as data points plotted at  $F_{\text{lat,p}} = F_{\text{lat,f}} = 0$  kN. Each simulated test is visualized by a small circular marker and the markers are interconnected by lines to display contours of the peak and quasi failure surfaces. The thin dashed lines show the area in which  $F_{\text{long}}^{\text{pre}}$  exceeds the limit given by (52). Moreover, results from experiments visualized by large markers are also displayed in Figures 7 and 8. It is seen that there are a fair agreement between simulations and experimental data.

It should be remarked that the magnitude of the plastic deformations at quasi failure are larger in the mixed lateral resistance tests than in the longitudinal resistance tests

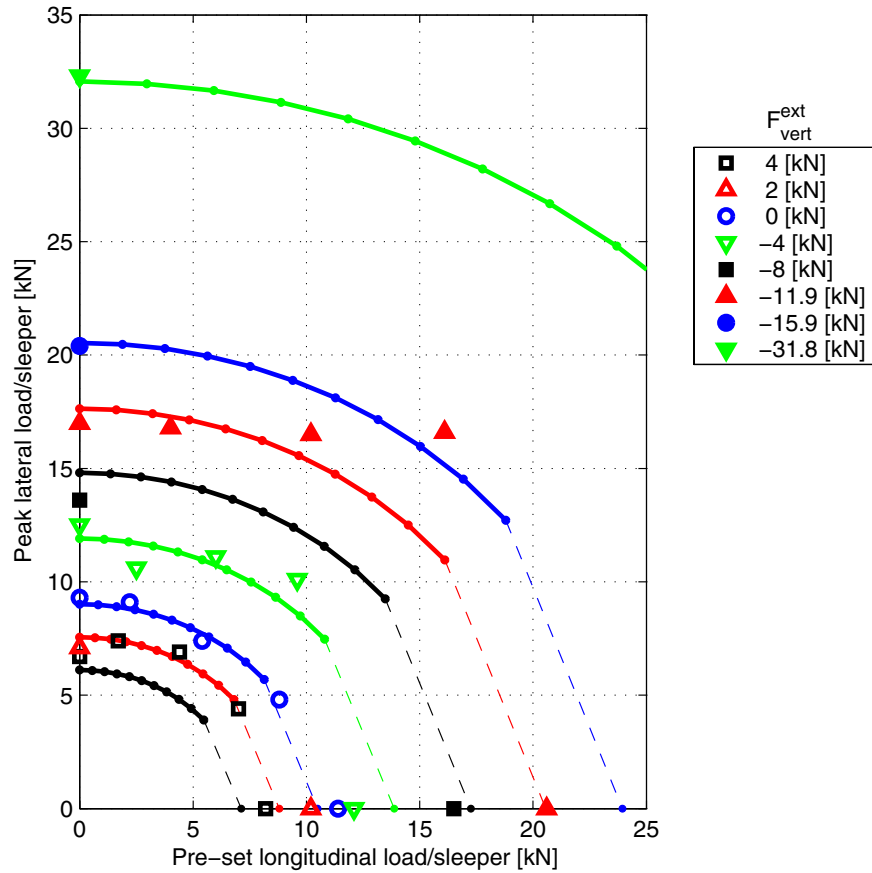


**Figure 7** Results of model simulations (solid lines) and experiments (markers) showing peak lateral ballast resistances longitudinal loads together with peak longitudinal resistances ( $F_{\text{lat,p}} = 0$  kN) for various constant vertical loads. The dashed lines denote the regions of not feasible loading.

implying different amount of softening. The results from the two test types shown in Figure 8 are not directly comparable, which make results presentation somewhat awkward.

The lateral deformations at peak resistance have been computed. The results from computations together with experimentally obtained values are shown in Figure 9. It is seen that there is a large scatter in the experimental data which makes the comparison inconclusive. The large scatter in the test results may be due to the difficulties to reproduce the same initial track condition before each test, such as ballast compaction, sleeper embedment within the ballast and track geometries. Moreover, the consolidation level corresponded to a weak track which means that the ballast resistance curve has not a distinctive peak which makes it difficult to determine the displacement corresponding to the peak resistance.

The longitudinal displacement at lateral quasi failure for the various pre-set longitudinal forces and vertical loads, that was used in the experiments (test types a and c), has been computed and is shown in Figure 10 together with results from experiments. It is seen that the model predicts the experimental results fairly well when  $a^* / a = 0.7$ , i.e. when a

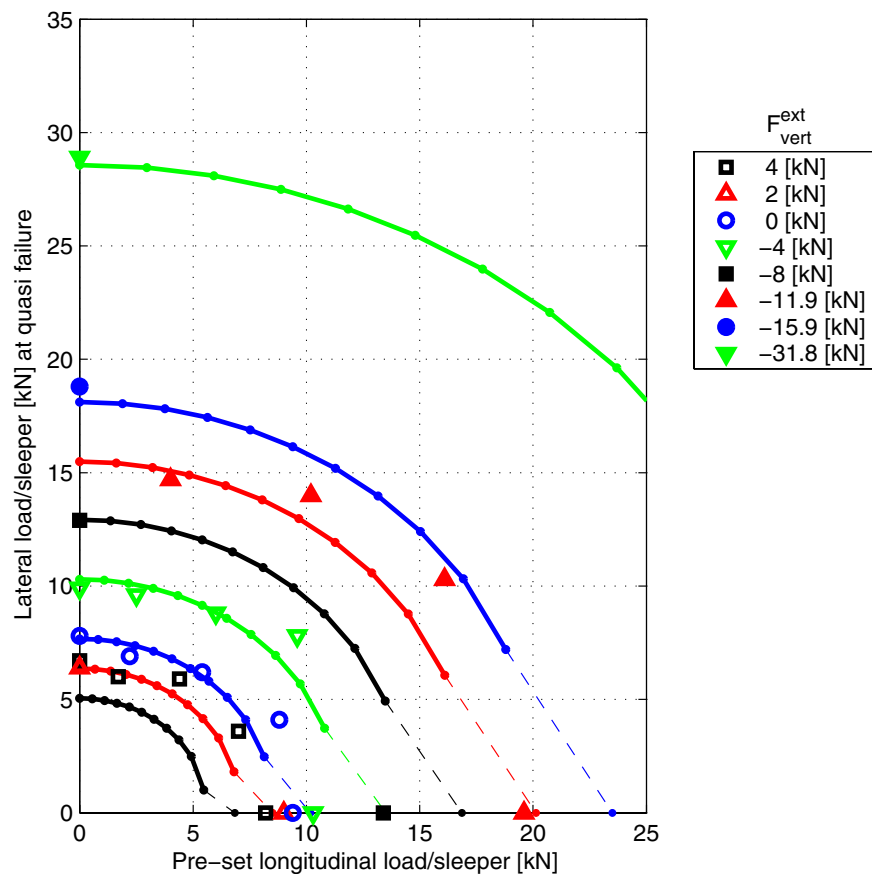


**Figure 8** Results of model simulations (solid lines) and experiments (markers) showing the lateral ballast resistances at quasi failure ( $u_{lat} = 0.2$  m) for different pre-set longitudinal loads and for various constant vertical loads. Markers at  $F_{lat,f} = 0$  kN denote longitudinal resistances at quasi failure. The dashed lines denote the region not feasible loading.

non-associative plastic flow in the plane of transversal displacements is assumed, but overestimates the longitudinal displacements when associativity is assumed, i.e. when  $a^* / a = 1$ .

Model simulations yielding vertical displacement at quasi failure are shown in Figure 11. The simulations are carried out using  $a^* / a = 0.7$ . It is seen that the vertical displacement becomes larger for a combined lateral and longitudinal loading, which is expected.

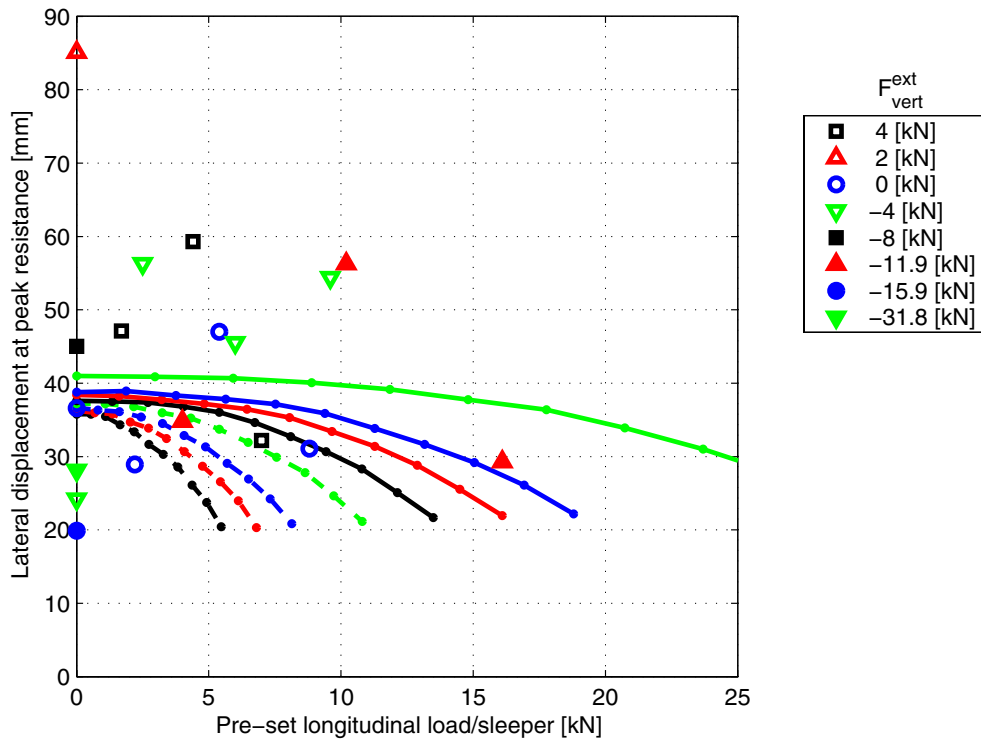


**Figure 9** Lateral displacement at peak resistance for test types a and c. Results from simulations are shown as dashed lines for  $F_{\text{vert}} = \{4, 2, 0, -4\}$  kN and solid lines for  $F_{\text{vert}} = \{-8, -11.9, -15.9, -31.8\}$  kN. The markers are results from experiments.

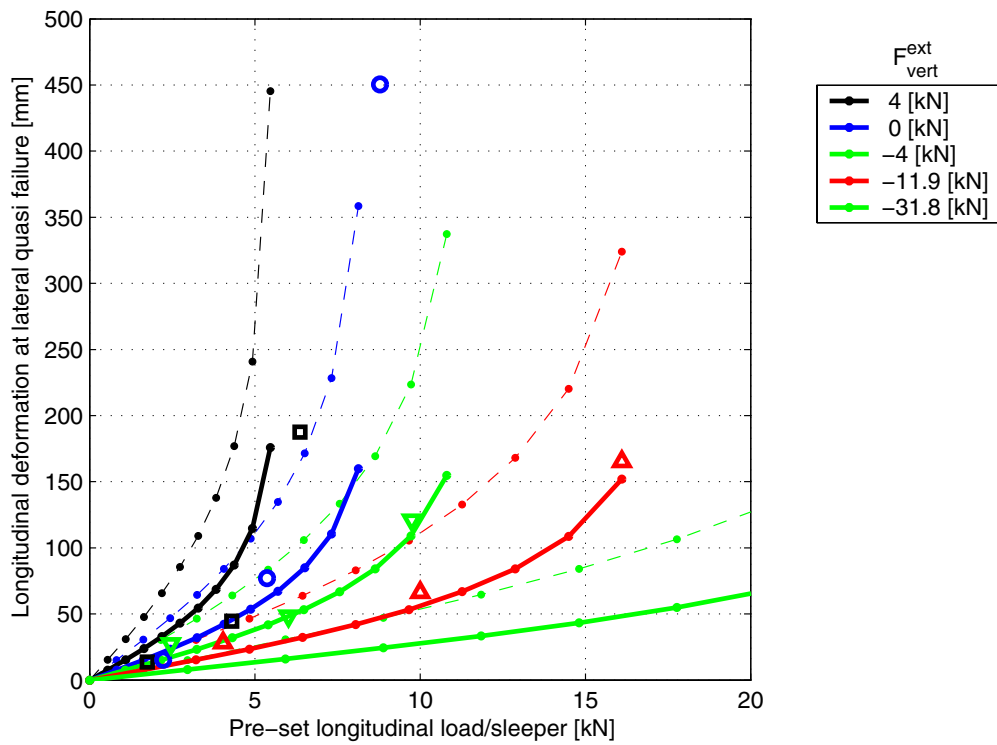


**Figure 10** Longitudinal displacement at lateral quasi failure for test types a and c. Results of model simulations for  $a^*/a = 0.7$  (thick solid lines) and  $a^*/a = 1$  (thin dashed lines) and experiments (markers).

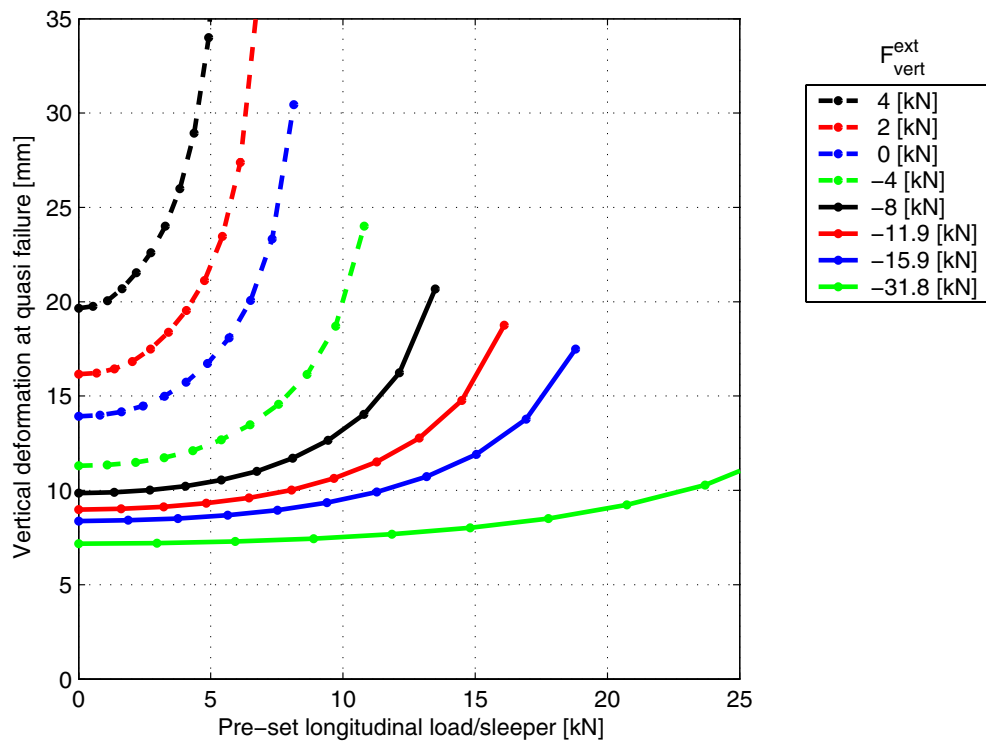


**Figure 11** Computed vertical displacement at quasi failure for test types a and c.

## 5 Discussion and conclusions

A plasticity model that can represent ballast resistance has been developed. The model is expressed in terms of structural variables, namely sleeper displacements and forces acting on the sleeper. The yield function of Drucker-Prager type together with a non-associative flow rule was found to be suitable in order to obtain good agreement with experimental data. The constitutive equations were integrated using the implicit Backward Euler rule. Moreover, detailed derivations of the linearized incremental equations are presented.

A procedure for model calibration was proposed. Results from lateral ballast resistance tests conducted with various constant vertical load levels were first used to determine a sub-set of the model parameters. The remaining parameters were determined using data from ballast resistance tests conducted with various constant vertical load levels. The prediction capability of the model was demonstrated using data from tests carried out with mixed lateral and longitudinal loading for various levels of constant vertical loads. An alternative way would be to use the experimental data from all tests simultaneously and determine all parameters in one calibration routine. However, each iteration step in the calibration procedure would be computer consuming.

A further development of the model should include implementation of a non-linear elastic law in the vertical direction. Moreover, the development of vertical plastic deformations should be capped as the vertical deformations can grow unlimited with the current flow rule, which is unrealistic. This situation could be seen in Figure 11 in the cases when the pre-set longitudinal load was close to failure yielding large transversal plastic deformations. However, it may not significantly affect the results in a buckling simulation of a real track, but it is recommended that it has to be checked.

Data from ballast resistance tests with mixed loadings are scarce. Additional tests on tracks with various type of materials, degree of consolidation and geometries are needed in order to widen the range of track types that can properly be analysed. However, it was seen from the used experiments that there sometimes was a large scatter in the results, which indicates a difficulty to reproduce the tests.

## References

- [1] Bao Y L, Three dimensional stability/lateral shift analysis of continuous welded rail (CWR) track and innovative methods to enhance CWR track performance, PhD Thesis, University of Illinois, 1998, 281 pp
- [3] Cannmo P, A damage-based interface model: Application to the degradation of and failure of polycrystalline microstructure, PhD Thesis, Chalmers University of Technology, 1997, 160 pp
- [4] Dogneton, P, The experimental determination of the axial and lateral track-ballast resistance, *Railroad Track Mechanics & Technology*, Princeton University, New Jersey, ISBN 0-08-021923-3, 1975
- [5] Donley M G, Kerr A D, Thermal buckling of curved railroad tracks, *International Journal of Non-Linear Mechanics*, v 22, n 3, 1987, pp 175-192
- [6] El-Ghazaly H A, Sherbourne A N & Arbabi F, Strength and stability of railway tracks – II, Deterministic, finite element stability analysis, *Computers & Structures*, v 39, n 1/2, 1991, pp 23-45
- [7] ERII D 202/DT 362: Improved knowledge of forces in CWR track (including switches): Ballast resistance under three-dimensional loading, April 1997, 52 pp
- [8] ERII D 202/RP 2: Improved knowledge of forces in CWR track (including switches): Review of existing experimental work on behaviour of CWR track, Provisional report, February 1995, 17 pp
- [9] ERII D 202/RP 3: Improved knowledge of forces in CWR track (including switches): Theory of CWR track stability, February 1995, 168 pp
- [10] ERII D 202/RP 4: Improved knowledge of forces in CWR track (including switches): Stability of continuous welded track, March 1999, 195 pp
- [11] ERII D 202/RP 7: Improved knowledge of forces in CWR track (including switches): Lateral and longitudinal resistance measurements: synthesis report, April 1999, 17 pp
- [12] Jacobsson L. User element for ABAQUS designed to represent ballast resistance, SP Technical Notes 2005:12, Building Technology and Mechanics, SP Swedish National and Testing and Research Institute, Borås, 2005, 9 pp
- [13] Kabo E, Ekberg A and Jacobsson L. Railway track stability – a state-of-the-art survey, Research Report 2004:2, Department of Applied Mechanics, Chalmers University of Technology, Gothenburg, Sweden, 2004, 94 pp
- [14] Kerr A D, An improved analysis for thermal track buckling, *International Journal of Non-Linear Mechanics*, v 15, 1980, pp 99-114
- [15] Kerr A D, The effect of lateral resistance on track buckling analyses, *Rail International*, n 1, 1976, pp 30-38



- [16] Kish A, Samavedam G, Wormley D, Fundamentals of Track Lateral Shift for High-Speed Rail Applications, Presented at the European Rail Research Institute's Interactive Conference on "Cost Effectiveness and Safety Aspects of Railway Track," Paris, France, December 8-9, 1998, 25 pp
- [17] Kish A, Samavedam G, Wormley D, New Track Shift Safety Limits for High-Speed Rail Applications, *Proceedings of World Congress on Railway Research*, Cologne, Germany, November 2001, 20 pp
- [18] Kish A, Recent results in track buckling research, AREA, American Railway Engineering Association, Bulletin 716, v 89, 1988, pp 281-296
- [19] Miura, Shigeru, Lateral track stability: theory and practice in Japan, *Transportation Research Record* 1289, 1991, pp 53-63
- [20] Oscarsson J, Dynamic train-track interaction, PhD Thesis, Department of Solid Mechanics, Chalmers University of Technology, 2001
- [21] Samavedam G, Kish A, Jeong D, Parametric studies on lateral stability of welded rail track, Report no DOT/FRA/ORD-83/07, U.S. Department of Transportation Research and Special Programs Administration, Transportation Systems Center, May 1983, 60 pp
- [22] Samavedam G, Kish A, Purple A and Schoengart J, Parametric analysis and safety concepts of CWR track buckling mechanics, DOT/FRA/ORD-93 /26 || DOT-VNTSC-FRA-93-25, US Department of Transportation Volpe Center, Railroad Systems Division, 1993, 120 pp
- [23] Samavedam G, Kish A, Continuous welded rail track buckling safety assurance through field measurements of track resistance and rail force, *Transportation Research Record* 1289, 1991, pp 39-52
- [24] Selig E T, Waters J M, Track geotechnology and substructure management, Thomas Telford, 1994, 446 pp
- [25] Sussmann T, Kish A, Trosino M, Investigation of the Influence of Track Maintenance on the Lateral Resistance of Concrete Tie Track, Transportation Research Board Conference, January 2003, 18 pp
- [26] Van M A, Stability of continuous welded rail track, PhD Thesis, Delft University of Technology, 1997, 180 pp
- [27] Zarembski A M & Magee G M, An investigation of railroad maintenance practices to prevent track buckling, AREA, American Railway Engineering Association, Bulletin 684, v 83, 1982, pp 1-61

## Appendix A

Inserting (7) and (13) to (y8) in the dissipation inequality (5) yields

$$D = \boldsymbol{\mu} \mathbf{F}^T \mathbf{f}^* = \boldsymbol{\mu} [F_{\text{lat}} f_{\text{lat}}^* + F_{\text{long}} f_{\text{long}}^* + F_{\text{vert}} f_{\text{vert}}^*] \geq 0 \quad (\text{A1})$$

By inserting (B1) to (B3) in (A1) and using (15) we obtain

$$D = \frac{2\boldsymbol{\mu}}{k_{\text{vert}}} [(F_e^*)^2 + F_{\text{vert}} (M^*)^2 F_{\text{vert}}^*] \geq 0 \quad (\text{A2})$$

The inequality (A2) is directly fulfilled when  $F_{\text{vert}} \geq 0$  as  $k_{\text{vert}} > 0$  and  $F_{\text{vert}}^* > 0$ .

Consider now the case when  $F_{\text{vert}} < 0$ . From (B4) follows

$$F_{\text{vert}}^* = \sqrt{\left(\frac{F_e^*}{M^*}\right)^2 + F_0^2} < \frac{F_e^*}{M^*} + F_0 \quad (\text{A3})$$

Insertion of (A3) in (A2) yields

$$D = \frac{2\boldsymbol{\mu}}{k_{\text{vert}}} [(F_e^*)^2 + F_{\text{vert}} (M^*)^2 F_{\text{vert}}^*] > \frac{2\boldsymbol{\mu}}{k_{\text{vert}}} \bar{D} \geq 0 \quad (\text{A4})$$

where

$$\bar{D} = \left[ (F_e^*)^2 + F_{\text{vert}} (M^*)^2 \left( \frac{F_e^*}{M^*} + F_0 \right) \right] \quad (\text{A5})$$

Hence, it suffices to check that  $\bar{D} \geq 0$  in order to fulfil (A1). From (9) follows that

$$F_e = -M(F_{\text{vert}} - F) - c \quad (\text{A6})$$

holds at plastic yielding. We may look at two extremes, when  $F_{\text{long}} = 0$  and when

$F_{\text{lat}} = 0$ , respectively. All other load combinations will lie in between the studied cases.

Starting with the case  $F_{\text{lat}} = 0$ , we observe from (10) and (15) that

$$F_e^* = \frac{a^*}{a} F_e \quad (\text{A7})$$

Inserting (A6) and (A7) in (A5) yields

$$\bar{D}(F_{\text{vert}}) = C_1 (F_{\text{vert}})^2 + C_2 F_{\text{vert}} + C_3 \quad (\text{A8})$$

where

$$C_1 = \frac{a^*}{a} M \left( \frac{a^*}{a} M - M^* \right) \quad (\text{A9})$$

$$C_2 = (M^*)^2 F_0 - \frac{a^*}{a} (MF_c - c) \left( \frac{a^*}{a} 2M - M^* \right) \quad (\text{A10})$$

$$C_3 = \left( \frac{a^*}{a} \right)^2 (MF_c - c)^2 \quad (\text{A11})$$

The function  $\bar{D}$  has its minimum when

$$\frac{d\bar{D}(F_{\text{vert}})}{dF_{\text{vert}}} = 2C_1 F_{\text{vert}} + C_2 = 0 \quad \Rightarrow \quad F_{\text{vert}} = -\frac{C_2}{2C_1}$$

This yields

$$\bar{D}_{\text{min}} = C_3 - \frac{C_2^2}{4C_1} \quad (\text{A12})$$

The second case to check is when  $F_{\text{long}} = 0$ . We conclude from (10) and (15) that

$$F_e^* = F_e \quad (\text{A13})$$

Following the same procedure as stated above leads to (A12) in which  $a^*/a = 1$  in (A9) to (A11). By inserting the actual parameter values listed in Table 2 in section 4.2, we see that  $C_1 > 0$  and  $C_3 > 0$  in both investigated cases. We thereby conclude that the dissipation inequality (A1) is unconditionally fulfilled with the current parameter settings.

## Appendix B

The gradients of the plastic potential surface  $\phi^*$  given in (y5) are

$$f_{\text{lat}}^* = \frac{2F_{\text{lat}}}{k_{\text{vert}}} \quad (\text{B1})$$

$$f_{\text{long}}^* = \frac{2(a^*)^2 F_{\text{long}}}{k_{\text{vert}}} \quad (\text{B2})$$

$$f_{\text{vert}}^* = \begin{cases} 0 & , M^* = 0 \\ \frac{2(M^*)^2 [F_{\text{c}}^* - F_{\text{vert}} + F_0]}{k_{\text{vert}}} = \frac{2(M^*)^2 F_{\text{vert}}^*}{k_{\text{vert}}} & , M^* \neq 0 \end{cases} \quad (\text{B3})$$

where (16) was used in (y8) and where

$$F_{\text{vert}}^* = \sqrt{\left(\frac{F_{\text{e}}^*}{M^*}\right)^2 + F_0^2} \quad (\text{B4})$$

was introduced. We will henceforth only study the case when  $M^* \neq 0$ .

As to the components in the Jacobian matrix (28) pertinent to the gradients of  $\phi^*$  we have

$$\frac{df_{\text{lat}}^*}{du_{\text{lat}}^{\text{e}}} = \frac{\partial f_{\text{lat}}^*}{\partial F_{\text{lat}}} \frac{dF_{\text{lat}}}{du_{\text{lat}}^{\text{e}}} = \frac{2k_{\text{lat}}}{k_{\text{vert}}} \quad (\text{B5})$$

$$\frac{df_{\text{long}}^*}{du_{\text{long}}^{\text{e}}} = \frac{\partial f_{\text{long}}^*}{\partial F_{\text{long}}} \frac{dF_{\text{long}}}{du_{\text{long}}^{\text{e}}} = \frac{2(a^*)^2 k_{\text{long}}}{k_{\text{vert}}} \quad (\text{B6})$$

$$\frac{df_{\text{vert}}^*}{du_{\text{lat}}^{\text{e}}} = \frac{\partial f_{\text{vert}}^*}{\partial F_{\text{vert}}} \frac{\partial F_{\text{vert}}^*}{\partial F_{\text{lat}}} \frac{dF_{\text{lat}}}{du_{\text{lat}}^{\text{e}}} = \frac{2F_{\text{lat}} k_{\text{lat}}}{F_{\text{vert}}^* k_{\text{vert}}} \quad (\text{B7})$$

$$\frac{df_{\text{vert}}^*}{du_{\text{long}}^{\text{e}}} = \frac{\partial f_{\text{vert}}^*}{\partial F_{\text{vert}}} \frac{\partial F_{\text{vert}}^*}{\partial F_{\text{long}}} \frac{dF_{\text{long}}}{du_{\text{long}}^{\text{e}}} = \frac{2(a^*)^2 F_{\text{long}} k_{\text{long}}}{F_{\text{vert}}^* k_{\text{vert}}} \quad (\text{B8})$$

Furthermore, the derivatives of  $\phi$  in (28) are

$$\frac{d\phi}{du_{\text{lat}}^{\text{e}}} = \frac{dF_{\text{e}}}{du_{\text{lat}}^{\text{e}}} + \frac{dM}{d\kappa} \frac{d\kappa}{du_{\text{lat}}^{\text{e}}} (F_{\text{vert}} - F_{\text{c}}) \quad (\text{B9})$$

$$\frac{d\phi}{du_{\text{long}}^{\text{e}}} = \frac{dF_{\text{e}}}{du_{\text{long}}^{\text{e}}} + \frac{dM}{d\kappa} \frac{d\kappa}{du_{\text{long}}^{\text{e}}} (F_{\text{vert}} - F_{\text{c}}) \quad (\text{B10})$$

$$\frac{d\phi}{du_{\text{vert}}^{\text{e}}} = M k_{\text{vert}} \quad (\text{B11})$$

$$\frac{d\phi}{d\Delta\mu} = \frac{dM}{d\kappa} \frac{d\kappa}{d\Delta\mu} = M'(\kappa) f_{\kappa}^* \quad (\text{B12})$$

where

$$\frac{dF_e}{du_{\text{lat}}^e} = \frac{F_{\text{lat}}}{F_e} k_{\text{lat}}$$

$$\frac{dF_e}{du_{\text{long}}^e} = \frac{a^2 F_{\text{long}}}{F_e} k_{\text{long}}$$

and (11) yields

$$M'(\kappa) = \frac{dM}{d\kappa} = \begin{cases} (M_p - M_i) \frac{n}{\kappa_p} (1 - \kappa/\kappa_p)^{n-1}, & (0 \leq \kappa/\kappa_p \leq 1) \\ - \frac{(M_p - M_f)^2}{[M_p - M_f + H(\kappa/\kappa_p - 1)]^2} \frac{H}{\kappa_p}, & (\kappa/\kappa_p > 1) \end{cases}$$

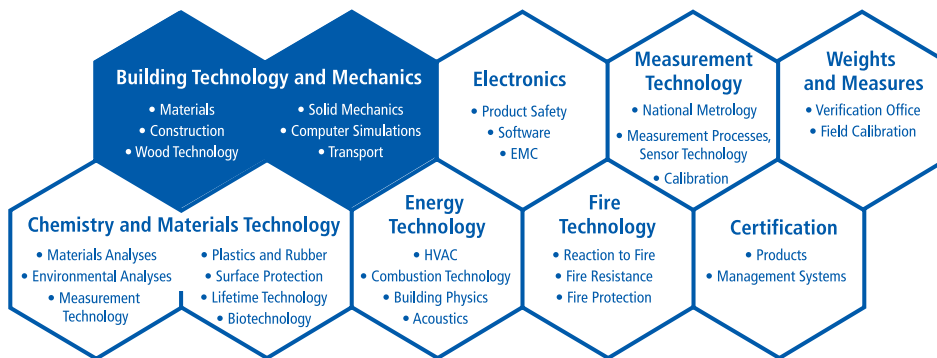
Moreover, from (18) follows

$$\frac{d\kappa}{du_{\text{lat}}^e} = \Delta\mu \frac{df_{\kappa}^*}{df_{\text{lat}}^*} \frac{df_{\text{lat}}^*}{du_{\text{lat}}^e} = \frac{\Delta\mu f_{\text{lat}}^*}{[(f_{\text{lat}}^*)^2 + (f_{\text{long}}^*)^2]^{1/2}} \frac{df_{\text{lat}}^*}{du_{\text{lat}}^e}$$

$$\frac{d\kappa}{du_{\text{long}}^e} = \Delta\mu \frac{df_{\kappa}^*}{df_{\text{long}}^*} \frac{df_{\text{long}}^*}{du_{\text{long}}^e} = \frac{\Delta\mu f_{\text{long}}^*}{[(f_{\text{lat}}^*)^2 + (f_{\text{long}}^*)^2]^{1/2}} \frac{df_{\text{long}}^*}{du_{\text{long}}^e}$$

**SP Swedish National Testing and Research Institute** develops and transfers technology for improving competitiveness and quality in industry, and for safety, conservation of resources and good environment in society as a whole. With Swedens widest and most sophisticated range of equipment and expertise for technical investigation, measurement, testing and certification, we perform research and development in close liaison with universities, institutes of technology and international partners.

SP is a EU-notified body and accredited test laboratory. Our headquarters are in Borås, in the west part of Sweden.



SP Building Technology and Mechanics  
 SP REPORT 2005:27  
 ISBN 91-85303-58-5  
 ISSN 0284-5172



**SP Swedish National Testing and Research Institute**

Box 857  
 SE-501 15 BORÅS, SWEDEN  
 Telephone: + 46 33 16 50 00, Telefax: +46 33 13 55 02  
 E-mail: info@sp.se, Internet: www.sp.se

*A Member of*

